LA-7330-MS
Informal Report
c.3

UC-32
Issued: June 1978

Time-Resolved PHERMEX Image Restorations Constrained with an Additional Multiply-Exposed Image

R. P. Kruger
J. R. Breedlove, Jr.
H. J. Trussell

LOS ALAMOS SCIENTIFIC LABORATORY
Post Office Box 1663 Los Alamos, New Mexico 87545

An Affirmative Action/Equal Opportunity Employer

UNITED STATES
DEPARTMENT OF ENERGY
CONTRACT W-7405-ENG. 36

TIME-RESOLVED PHERMEX IMAGE RESTORATIONS CONSTRAINED WITH AN ADDITIONAL MULTIPLY-EXPOSED IMAGE

by

R. P. Kruger
J. R. Breedlove, Jr.
H. J. Trussell

ABSTRACT

There are a number of possible industrial and scientific applications of nanosecond cineradiographs. Although the technology exists to produce closely spaced pulses of x rays for this application, the quality of the time-resolved radiographs is severely limited. The limitations arise from the necessity of using a fluorescent screen to convert the transmitted x rays to light and then using electro-optical imaging systems to gate and to record the images with conventional high-speed cameras. It has been proposed that in addition to the time-resolved images, a conventional multiply-exposed radiograph be obtained. This report uses both PHERMEX and conventional photographic simulations to demonstrate that the additional information supplied by the multiply-exposed radiograph can be used to improve the quality of digital image restorations of the time-resolved pictures over what could be achieved with the degraded images alone.

I. INTRODUCTION

Recent studies related to improving PHERMEX radiography raised an interesting image-processing question. Could a multiply-exposed, but otherwise undegraded, image be used to improve the quality of digital restorations of degraded versions of the individual scenes in the multiple image? Since the multiple exposure is additional information, the intuitive answer is "yes!" We describe an algorithm to use the additional information in the multiple exposure to improve the restorations beyond those possible with only the degraded images and knowledge of the degrading function and image statistics.

One rarely finds an imaging experiment in which separate low-quality pictures are obtained along with a high-quality multiple exposure. PHERMEX is a 30-MeV electron accelerator used for flash (i.e., stop-action) radiography of rapidly moving objects. Advances in accelerator technology have made it possible to produce numbers of intense pulses of x rays which are closely spaced in time. With this capability ultra-high-speed cineradiography will be possible. It will be possible to produce at least three 40-ns bursts of radiation over a time span of between 4 and 1000 μs. Each radiation pulse would have an intensity of 100 R.

In a single-pulse flash radiography the usual image recording medium is film contained in special cassettes. Because of the size and weight of these cassettes, the film cannot be changed between the pulses. To take advantage of the multiple pulse capability being developed for the PHERMEX Facility, it was necessary to develop techniques for recording numbers of x-ray images closely spaced in time. The approach chosen was to convert the x-ray images into light images using a fluorescent screen. Light from the fluorescent screen is then recorded using a conventional high-speed, electronically intensified framing camera. Since the electro-optical camera imagery was poorer than conventional radiographs, digital image restoration was needed. The penetrating nature of x rays makes it possible to place a conventional x-ray film cassette between the object and the fluorescent screen. The image recorded on such a film would be the superposition of radiographs from each of the radiation pulses. Each component image would have the clarity of conventional PHERMEX radiography. The possibility of obtaining this additional image for each series of time-resolved radiographs motivated this study.

In this report we will present a model of the radiographic experiment from which simulations are derived. The simulations use both conventional photographs and actual PHERMEX simulations. An algorithm for restoration of the degraded images constrained by the multiply-explosed image will be derived. Experimental restorations of the simulated imagery will be presented. The work demonstrates the advantage of using the multiple exposure in the restoration scheme.

II. IMAGE MODEL AND SIMULATIONS

The degraded, time-resolved images are represented as the convolution of the undegraded images with a point-spread function. The noise is considered to be additive and signal-independent. Using matrix notation[1] the degraded image

is given by the expression

$$g_i = H f_i + n_0 , \qquad i = 1,2,\ldots N \tag{1}$$

where g_i represents the degraded image and f_i represents the input image. H is obtained from the point-spread function and n is the noise term. The multiple exposure is given by the expression

$$f_M = \sum_{i=1}^{N} f_i \quad . \tag{2}$$

For ordinary light photography the quantities f_i in Eq. (2) would be light intensities. For high-energy x rays recorded without fluorescent intensification screens the film density of the radiograph is proportional to the incident radiation intensity.[2] For x rays the f_i's in Eq. (2) could be film densities.

We initially used three conventional photographs of similar objects with large regions of relatively high density to simulate the f_i's. Figure 1 shows these three digitized images. The simulated point-spread function was a Gaussian with a standard deviation of 1.4 pixels. The noise function was a white, zero-mean Gaussian with a standard deviation of 0.04 density units. The signal-to-noise ratio was 20 dB. Figure 2 shows the simulation of one of the degraded images. Our motivation in this first study was to confirm the theoretical considerations to be developed using known and controllable degradations. Once this was done, the techniques were used to restore simulated PHERMEX images for which the degrading process can only be estimated.

III. RESTORATION ALGORITHM

One approach to restoring the degraded g_i's is to seek an estimate $\hat{f}_i$ which will minimize

$$\sum_{i=1}^{N} (g_i - H\hat{f}_i)^T (g_i - H\hat{f}_i) , \tag{3}$$

subject to the constraint

$$f_M = \sum_{i=1}^{N} \hat{f}_i \quad . \tag{4}$$

In these equations N is the number of degraded images. The solution is obtained using Lagrange multipliers. Minimize the quantity

$$s = \sum_{i=1}^{N} (g_i - H\hat{f}_i)^T (g_i - H\hat{f}_i) + \lambda^T \left(f_M - \sum_{i=1}^{N} \hat{f}_i \right) \tag{5}$$

with respect to the $\hat{f}_i$'s. λ^T is a row vector of N Lagrange multipliers. After carrying out the minimization of s and assuming that H^{-1} exists, the solution is

$$f_i = \frac{N-1}{N} H^{-1} g_i + \frac{1}{N} \left[f_M - \sum_{j \neq i=1}^{N} H^{-1} g_j \right] . \tag{6}$$

While the existence of H^{-1} could be questioned, Eq. (6) is very easy to derive and analyze. This expression for $\hat{f}_i$ is the essence of this paper. The solution is very satisfying intuitively. If N were 1, then the undegraded "multiple" image is the solution. As N increases, our ability to unscramble the multiple image decreases. Therefore, we rely more on the straightforward restoration for the solution. One would expect that in regions where the restorations of the other images are poor, residuals will remain in the second term. These residuals appear as "ghosts" in the constrained restorations. These are particularly evident in high-contrast regions of the images. Ghosts will be unavoidable if imperfect global processing is used.

The following derivations show that the form of Eq. (6) holds for other restoration schemes. Let $\hat{f}_i$ be a linear combination of some arbitrary restoration $\mathcal{R}(g_i)$ and the difference $[f_M - \sum_{j \neq i} \mathcal{R}(g_i)]$. Let Eq. (4) be a constraint.

$$\hat{f}_i = \alpha \mathcal{R}(g_i) + \beta \left[f_M - \sum_{j \neq i} \mathcal{R}(g_i) \right] . \tag{7}$$

Sum the $\hat{f}_i$'s to obtain

$$f_M = \sum_{i=1}^{N} \hat{f}_i = \alpha \sum_{i=1}^{N} \mathcal{R}(g_i) + \beta N f_M - \beta(N-1) \sum_{i=1}^{N} \mathcal{R}(g_i) ; \tag{8}$$

consequently, $\beta = 1/N$ and $\alpha = (N-1)/N$.

Now consider the restoration which minimizes the expected value of the total error between the f_i's and the $\hat{f}_i$'s.

$$\text{Minimize:} \qquad E\left\{\sum_{i=1}^{N}[f_i - \hat{f}_i]^T[f_i - \hat{f}_i]\right\} , \tag{9a}$$

where E{...} is the expected value. Substituting Eq. (7) into Eq. (9a) and assuming $\mathscr{R}(g_i) = Wg_i$, where W is a linear operator, one obtains the expression

$$\text{Minimize:} \qquad E\left\{\left|f_i - \frac{N-1}{N} Wg_i - \frac{1}{N} f_M + \frac{1}{N}\sum_{j\neq i=1}^{N} Wg_i\right|^2\right\} . \tag{9b}$$

If one expands the terms inside the summation, sums each term, differentiates with respect to W, and sets the result equal to zero, Eq. (9b) becomes

$$\begin{aligned} E\Bigg\{ & -\frac{2(N-1)}{N}\sum_{i=1}^{N} f_i g_i^T + \frac{2}{N}\sum_{i=1}^{N} f_i \sum_{j\neq 1} g_i^T \\ & + \frac{2(N-1)^2}{N^2}\sum_{i=1}^{N} Wg_i g_i^T + \frac{2(N-1)}{N^2} f_M \sum_{i=1}^{N} g_i^T \\ & - \frac{4(N-1)}{N^2} W \sum_{i=1}^{N} g_i \sum_{j\neq 1} g_i - \frac{2(N-1)}{N^2} f_M \sum_{i=1}^{N} g_i^T \\ & + \frac{2}{N^2} W \sum_{i=1}^{N}\left(\sum_{j\neq 1} g_j\right)\left(\sum_{j\neq 1} g_j^T\right)\Bigg\} = 0 . \end{aligned} \tag{10}$$

Multiplying Eq. (10) by N/2, factoring out W, and using the shorthand $g_M = \sum_{i=1}^{N} g_i$ one finds

$$E\left\{W\left[\sum_{i=1}^{N} g_i g_i^T - \frac{1}{N} g_M g_M^T\right]\right\} = E\left\{\sum_{i=1}^{N} f_i g_i^T - \frac{1}{N} f_M g_M^T\right\} . \tag{11}$$

Using Eq. (1) and assuming $E\{f_n^T\} = 0$, then $E\{f_i g_i^T\} = E\{f_i f_i^T H^T\}$. With the usual assumption that the images are independent and are drawn from a zero mean ensemble, then $E\{f_i f_j^T\} = 0$. If ergodicity holds, $E\{f_i f_i^T\} = E\{f_j f_j^T\}$. Therefore, subscripts can be dropped. W, the restoration filter that produces the minimum mean square error, is given by

$$W = \frac{E\{ff^T\}H^T}{H\,E\{ff^T\}H^T + E\{nn^T\}} = \frac{R_f\,H^T}{H\,R_f H^T + R_n}\,, \tag{12}$$

where R_f is the covariance matrix of f and R_n is the estimated noise covariance matrix. This is the standard Wiener filter often used in image processing. The filter which minimizes the mean square error for the N images with the constraint is the filter which minimizes the mean square error for each image separately.

As mentioned earlier, the three images shown in Fig. 1 were identically degraded to form the g_i images. Wiener restorations $R(g_i)$ and constrained restorations $\hat{f}_i$ based on unconstrained Wiener restorations were produced. Table I gives the mean square error between these two restorations and the original undegraded images f_i. Figures 3 and 4 show examples of Wiener and constrained restorations. The constrained outputs are superior in spite of the noticeable "ghost" residual images.

The results of $R(g_i)$ and $\hat{f}_i$ for Wiener, power spectrum equalization (PSE), and linear Maximum a Posteriori (MAP) restoration approaches will be used in the following sections using simulated PHERMEX radiographs. Our goal is to see how well the constrained restoration methods work on actual radiographic data.

IV. PHERMEX STUDIES

A. Spatial Calibration

In the previous section, the degraded images g_i were computer-generated from undegraded images f_i, and the superposition image f_M was the exact linear sum of f_i images (undegraded g_i images). By making these simplifications, several problems were avoided. First,

$$f_M = \sum_{i=1}^{N} f_i\,, \tag{13}$$

as was mentioned earlier. Second, since

$$g_i = Hf_i + n \quad , \tag{14}$$

the degrading process was well controlled and linear. Third, since f_M was the linear superposition of the f_i images, and g_i was a linear modification of f_i, the restored images $R(g_i)$ were of the same density range, digital resolution, and sampled identically to f_M. Lastly, it was possible to use the mean square error criterion to verify both the previously presented theory and the computer restoration algorithm.

The next logical step was to analyze actual PHERMEX-based simulations. To these ends four images were supplied to us by the PHERMEX group (M-2). Three of these were simulated time-resolved PHERMEX images, which were obtained by radiographing three spherical models of different radii through a time-gating electro-optic system. A fourth image consisted of a 36- by 53-cm PHERMEX superposition radiograph containing a triple exposure of these three models. Before Eq. (7) can be successfully applied to these radiographs, they have to be both spatially registered and densitometrically calibrated.

The three time-resolved images were scanned on the PDS microdensitometer using a 20-μm aperture. This resulted in a 1270 by 1270 image. The full-size multiple-exposure radiograph was digitized to 1250 by 1250 pixels using a 200-μm aperture. These raw images were not spatially registered and magnification of the full-size digitized radiograph differed from that of the time-resolved images. The density ranges were different, and no registration marks were available.

It was decided to use a previously developed circle-detection algorithm[3] to superimpose the centers of the individual spheres in the digitized time-resolved images. An example of the use of this algorithm is shown in Figs. 5a and 5b for two of the three time-resolved images. The superimposed circle is the best least squares estimate of the maximum chord length through the spherical shell. The spatial centroids of each image were also estimated. A similar process was undertaken for the superimposed image f_M as shown in Fig. 5c. Once the relative spatial centroids and radii for the four images were computed, they were translated to a common spatial center, and bilinear spatial interpolation was used to correct for magnification differences. Figures 6a and b show the computer superposition of the three time-resolved images and the triple-exposed image after centering and correcting for magnification differences.

One can see from the clarity of the grid pattern that the spatial registration is successful. The last step in the calibration process is yet to be undertaken. One should note the marked density differences between Figs. 6a and b. If Eq. (7) is to be successfully applied (i.e., ghost images resulting from the difference term minimized), f_M must reflect the same density range as $\sum^{N}\mathcal{R}(g_i)$. It is our intention to approximately map the densities present in f_M into those exhibited by $\sum^{N}\mathcal{R}(g_i)$. This density-modified f_M will then be used to restore the time-resolved images as indicated in Eq. (7).

B. Density Calibration

In the absence of a densitometrically calibrated step wedge on each g_i and f_M, the next best procedure involves the formation of a two-dimensional histogram of image densities. Figure 7 shows such a two-dimensional histogram. In this case the ordinate represents the summed image densities of $\sum_{i=1}^{3}\mathcal{R}(g_i)$ and the abscissa represents f_M. The darker the node, the greater the number of coincident gray-scale values between the two images. A piecewise linear single-valued mapping shown in Fig. 8 was passed through these major nodes to provide an approximate density mapping between $\sum\mathcal{R}(g_i)$ and f_M. The density matched f_M was then used in the constrained restorations to follow. Figure 9 shows a split-screen representation of the remapped f_M and $\Sigma(g_i)$. Appropriate visual defocus should convince one that the mapping is approximately correct. The diffuse nature of the histogram nodes is indicative of image noise as well as spatially variant densities. That is, PHERMEX beam misalignment caused spatially dependent density differences between the ideally spherical objects in the scene.

Several unconstrained restoration approaches were undertaken. Conventional Wiener restorations were very poor, because Wiener filters react strongly to high levels of image noise. These high noise levels produce substantial roll-offs in the filters at higher frequencies that are dominated by noise. Wiener restorations of these images appear blurred. More aggressive restoration techniques were needed. These will be discussed below. Our restoration experiments have also shown that the noise effects (n) dominated the blur effects (H) in the electro-optic system images.

Power Spectrum Equalization (PSE) makes the following assumption.[4] Let P_{f_i} and P_{g_i} be the power spectrum of f_i and g_i, respectively. The task is to constrain the restoration filter W such that the power spectrum of $\mathscr{R}(g_i)$ will equal that of f_i. Thus,

$$|W| = \left[\frac{P_{f_i}}{P_{g_i}} \right]^{1/2} . \tag{15}$$

In general, P_{f_i} is unknown. However, the ergodicity condition can be used to permit the estimation of the power spectrum P_{f_i} from a scene that is considered to be a member of the statistical ensemble to which g_i belongs. In the present case P_{f_M} of the less noisy superposition image is used as the prototype for each spectral equalization filter. Figure 10 shows two of the three original g_i images. Figure 11 shows the resultant $\hat{f}_i$ constrained restorations using PSE.

As a final approach, linear Maximum a Posteriori (MAP) restoration was undertaken.[5] The general form of the linear MAP restoration is given in Eq. (16).

$$\mathscr{R}(g) = (R_f^{-1} + H^T R_n^{-1} H)^{-1} (H^T R_n^{-1} g + R_f^{-1} \bar{f}) , \tag{16}$$

where R_f^{-1} and R_n^{-1} are inverse covariance matrices, and $\bar{f}$ is the mean vector of f. If $\bar{f} = 0$, one can see that this restoration is identical to the Wiener restoration of Eq. (12).

In practice, it has been shown that the covariance matrices can be well-approximated by scalars, that is, $R_f = \sigma_f^2 I$ and $R_n = \sigma_n^2 I$, where I is the identity matrix. The noise variance, σ_n^2, is easily estimated. The variance of the solution from the mean $\bar{f}$ is implicitly derived from the residual image, $r = g - Hf$, as shown in Ref. 5. The remaining unknown parameter $\bar{f}$ is usually approximated by the degraded image g itself. Experimental results have shown that the linear MAP filter gives results comparable to the Wiener filter with less a priori information. This filter is also less sensitive to perturbation of the estimated parameters than the Wiener filter. Figure 12 shows the MAP restoration of the images shown in Fig. 10.

V. CONCLUSIONS

In general, the results of Figs. 11 and 12 appear to be a mixed blessing. While it can be argued that the true edges appear more sharply defined, the residual "ghost" edges remain visible. This is partially a result of inaccurate or incomplete image subtraction [see Eq. (7)] due to the imprecision of the density remapping of f_M, and also the inability of $\mathcal{R}(g_i)$ restorations to match the edge characteristics of f_M. In observing the results, one is led to the conclusion that the latter reason dominates the former. It is, however, suggested that future work in this area include spatial registration marks on all films and some sort of physical density wedge phantom exposed with the films. In addition, attempts to minimize beam misalignment should be introduced in order to reduce spatial dependencies in the density remapping phase.

REFERENCES

1. H. C. Andrews and B. R. Hunt, Digital Image Restoration, (Prentice Hall, Inc., Englewood, New Jersey, 1977) Chap. 3.

2. R. H. Herz, The Photographic Action of Ionizing Radiations, (Wiley-Interscience, New York, New York, 1969).

3. R. L. Whitman, R. P. Kruger, R. H. Day, and D. M. Stupin, "Two-Dimensional Computer Modeling and Analysis of Thin-Walled Microspheres," Topical Meeting on Inertial Confinement Fusion, San Diego, California, February 1978.

4. T. M. Cannon, "Blind Deconvolution of Spatially Invariant Image Blurs with Phase," IEEE Trans. on Acoustics, Speech, and Signal Proc., Vol. ASSP-24, No. 1, February 1976.

5. H. J. Trussell, "Notes on Linear Image Restoration by Maximizing the A-Posteriori Probability," IEEE Trans. on Acoustics, Speech, and Signal Proc., July 1978.

Table I.

Comparison of Mean Square Errors
for Wiener and Constrained Restoration

$$MSE = \frac{1}{N^2} \sum_{i=1}^{N} \sum_{j=1}^{N} \left| f_{ij} - \hat{f}_{ij} \right|^2 .$$

Image Number	Mean Square Error	
	Wiener	Constrained
1	9.6×10^{-3}	5.0×10^{-3}
2	8.0×10^{-3}	4.6×10^{-3}
3	7.2×10^{-3}	3.8×10^{-3}

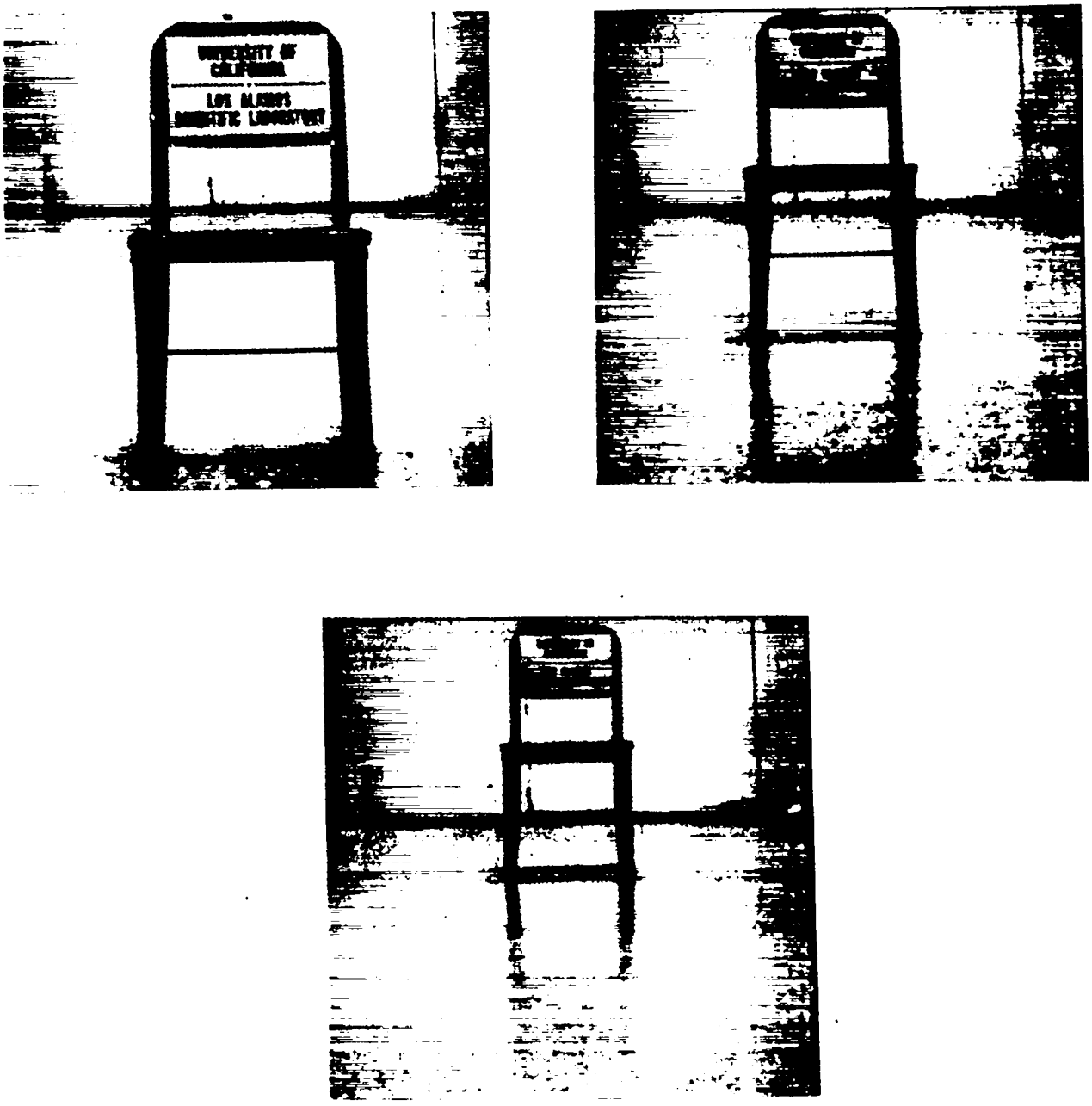

Fig. 1. Three undegraded original images.

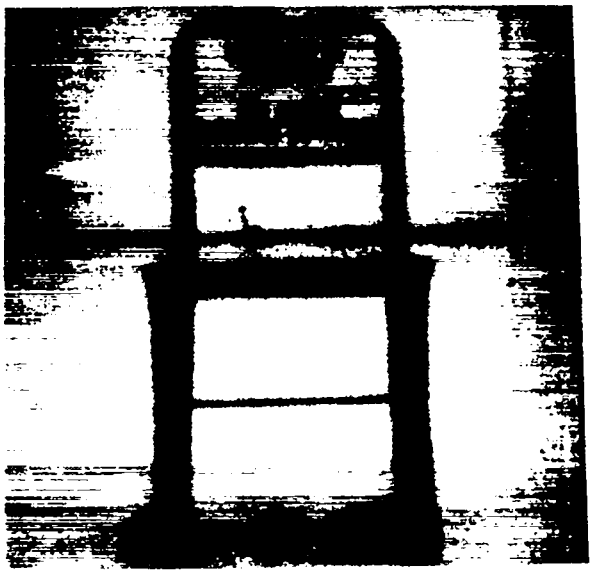

Fig. 2. Example of g_i noisy and defocused image.

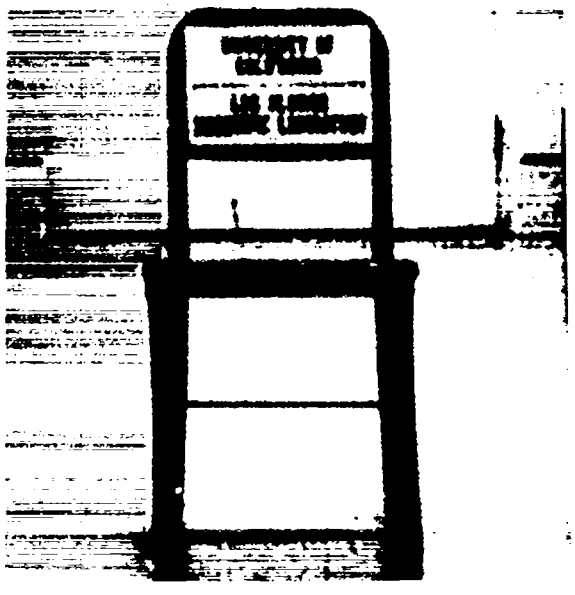

Fig. 3. Wiener restoration $\mathcal{R}(g_i)$ of image in Fig. 2.

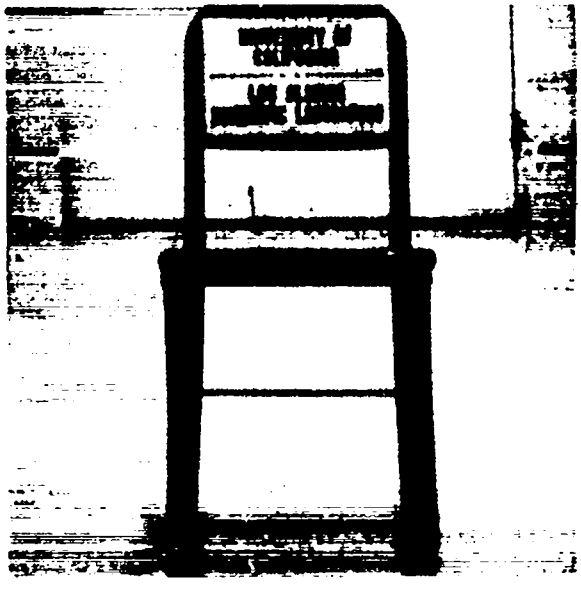

Fig. 4. Constrained restoration $\hat{f}_i$ corresponding to Figs. 2 and 3.

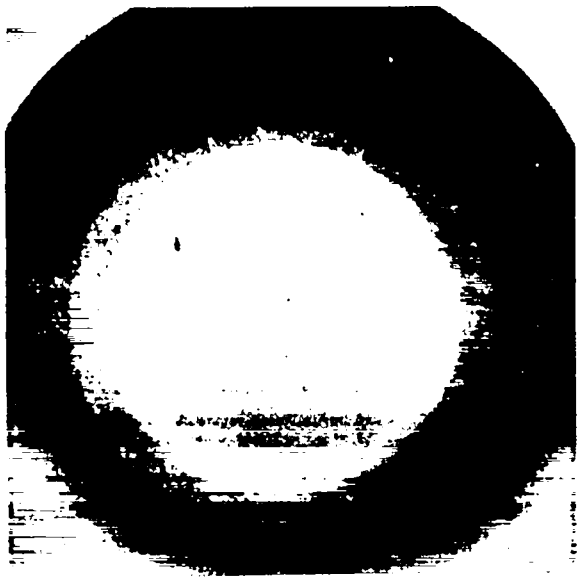

Fig. 5a. Circle detection of intermediate-sized sphere on g_2 image.

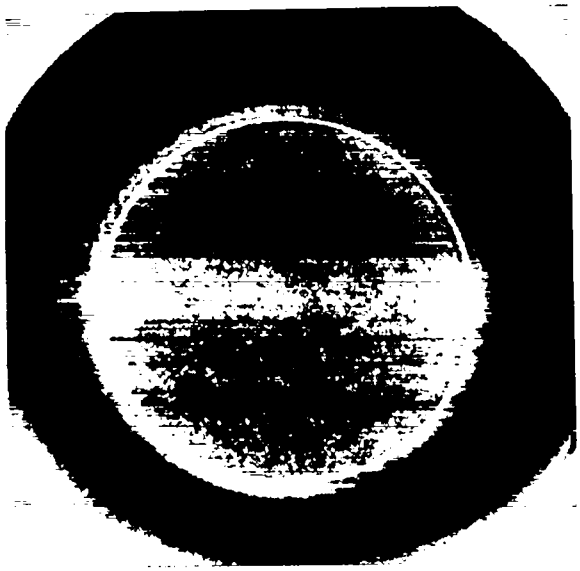

Fig. 5b. Circle detection of large-sphere image g_3.

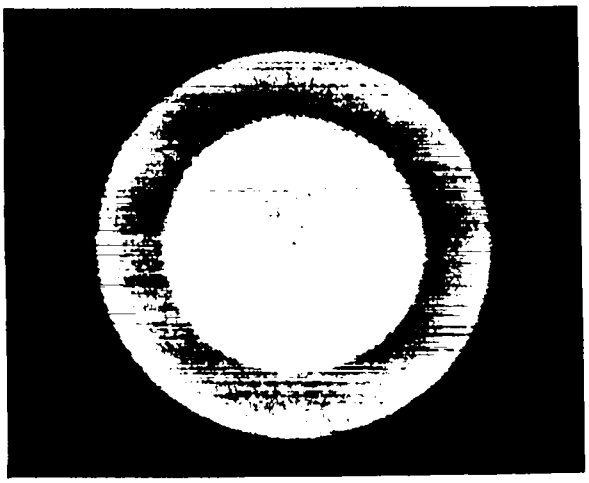

Fig. 5c. Circle detection of small-sized sphere on f_M.

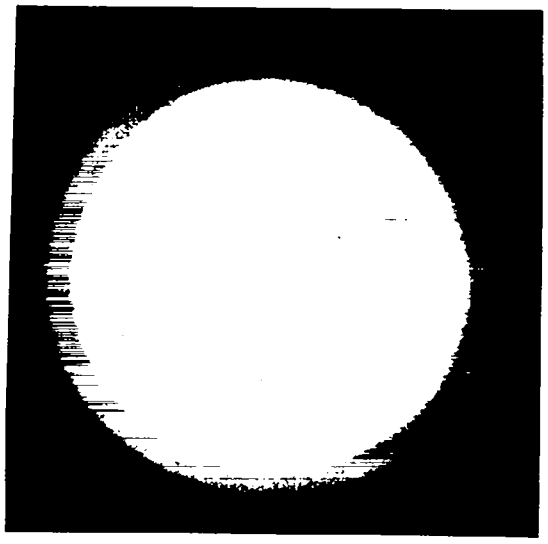

Fig. 6a. Superposition image f_M prior to density remapping.

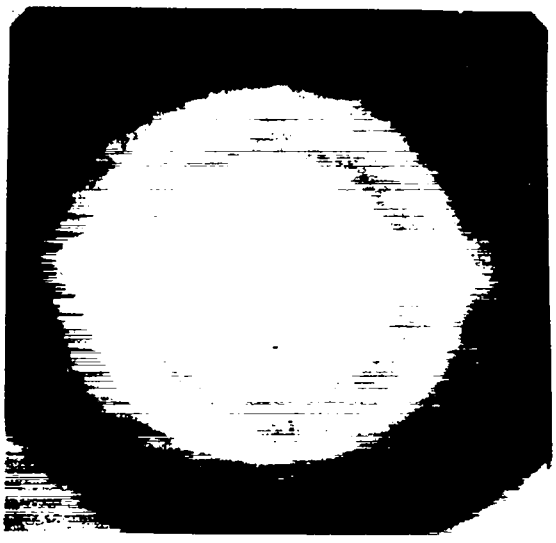

Fig. 6b. Superposition image Σg_i.

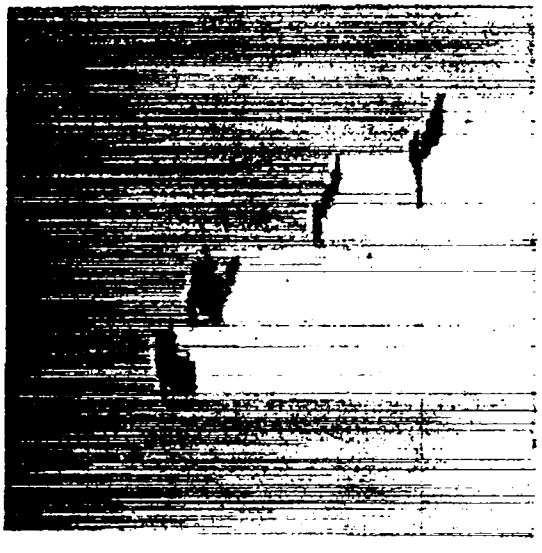

Fig. 7. Two-dimensional histogram abscissa (f_M), ordinate $[\Sigma \mathcal{R}(g_i)]$.

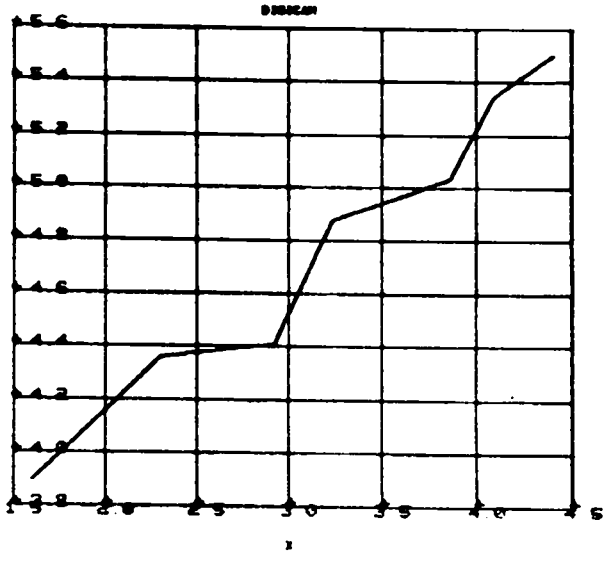

Fig. 8. Piecewise linear mapping corresponding to Fig. 7.

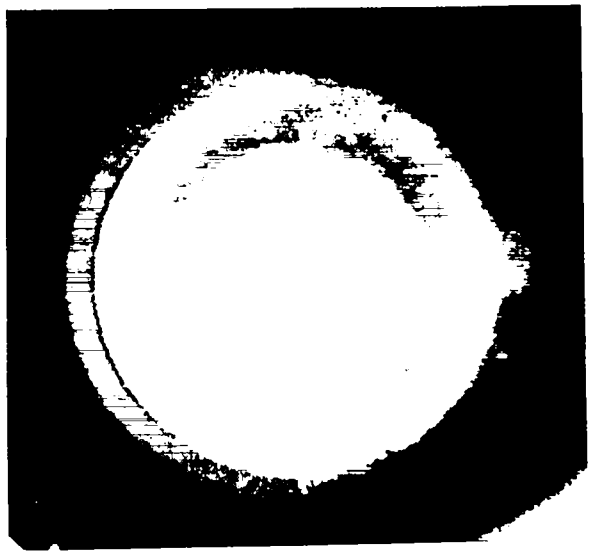

Fig. 9. Split screen image of density remapped f_M and $\Sigma(g_i)$.

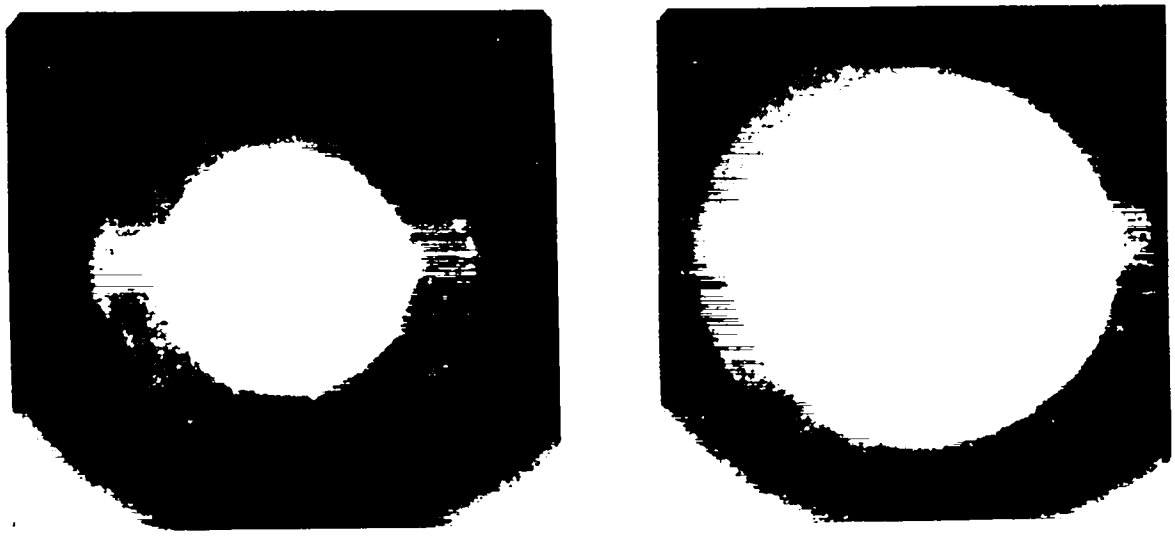

Fig. 10. Two of three degraded images (g_1, g_2).

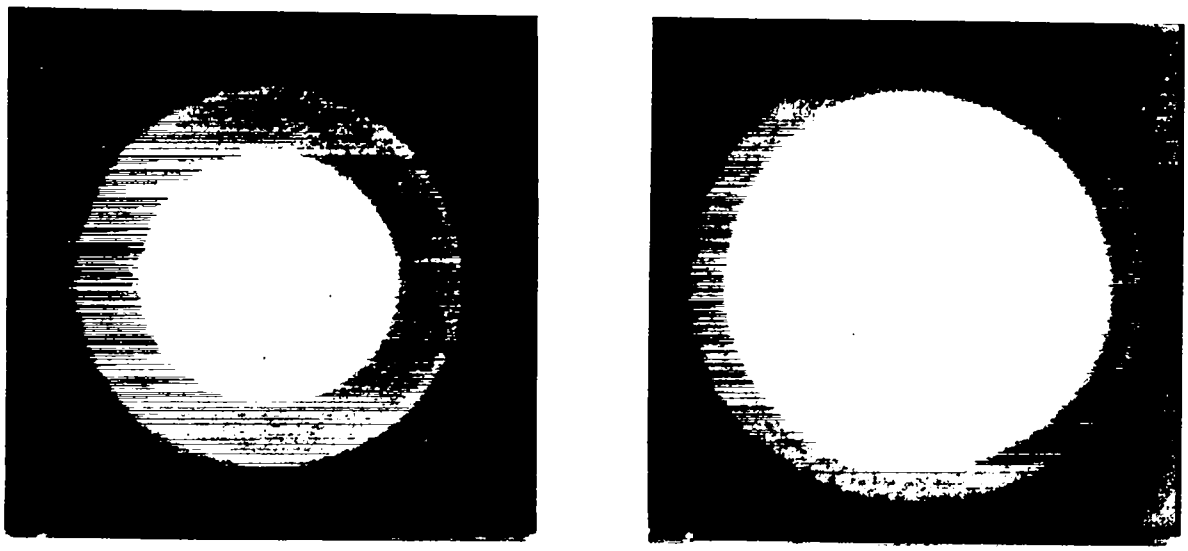

Fig. 11. Constrained restorations $\hat{f}_1$ and $\hat{f}_2$ using PSE.

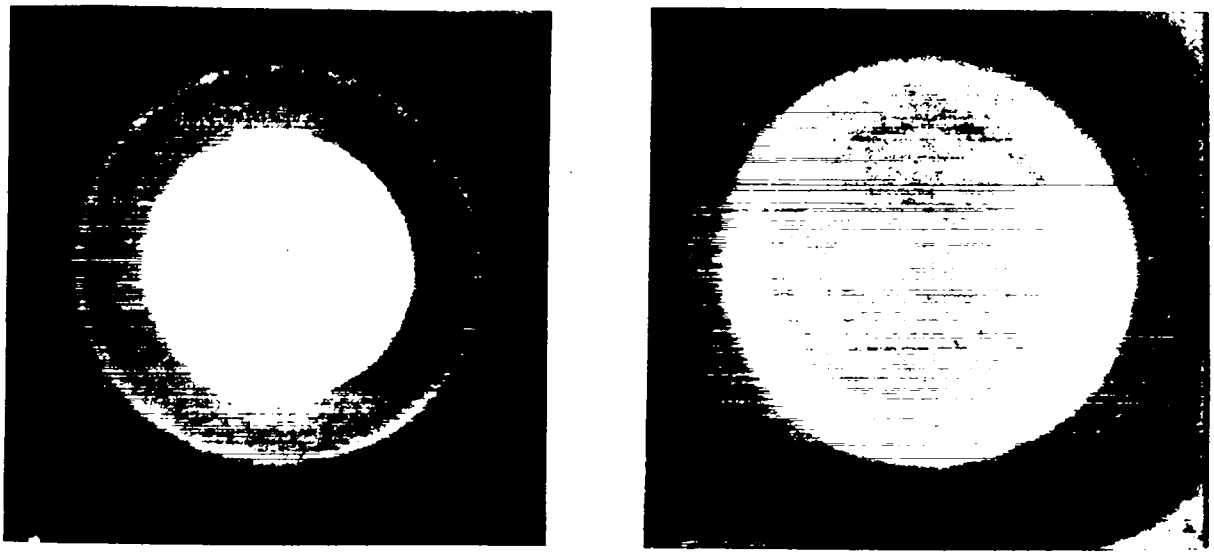

Fig. 12. Constrained restoration $\hat{f}_1$ and $\hat{f}_2$ using MAP.

Printed in the United States of America Available from
National Technical Information Service
U.S. Department of Commerce
5285 Port Royal Road
Springfield, VA 22161

Microfiche $ 3.00

001-025	4.00	126-150	7.25	251-275	10.75	376-400	13.00	501-525	15.25
026-050	4.50	151-175	8.00	276-300	11.00	401-425	13.25	526-550	15.50
051-075	5.25	176-200	9.00	301-325	11.75	426-450	14.00	551-575	16.25
076-100	6.00	201-225	9.25	326-350	12.00	451-475	14.50	576-600	16.50
101-125	6.50	226-250	9.50	351-375	12.50	476-500	15.00	601-up	--1

1. Add $2.50 for each additional 100-page increment from 601 pages up.